magnetochemistry

MDPI

Article

Magneto-Optic Surface Plasmon Resonance Ti/Au/Co/Au/P_c Configuration and Sensitivity

Conrad Rizal [1,2,*]

[1] Department of Electrical Engineering & Computer Science, York University, Toronto, ON M3J 1P3, Canada
[2] GEM Systems Inc., Markham, ON L3R 5H6, Canada

Received: 17 June 2018; Accepted: 13 August 2018; Published: 17 August 2018

Abstract: Magneto-optic surface plasmon resonance (MOSPR)-based sensors are highly attractive as next-generation biosensors. However, these sensors suffer from oxidation leading to degradation of performance, reproducibility of the sensor surface, because of the difficulty of removing adsorbed materials, and degradation of the sensor surface during surface cleaning and these limit their applications. In this paper, I propose MOSPR-based biosensors with 0 to 15 nm thick inert polycarbonate laminate plastic as a protective layer and theoretically demonstrate the practicability of my approach in water-medium for three different probing samples: ethanol, propanol, and pentanol. I also investigate microstructure and magnetic properties. The chemical composition and layered information of the sensor are investigated using X-ray reflectivity and X-ray diffraction analyses and these show distinct face-centered-cubic (fcc)-Au (111) phases, as dominated by the higher density of conduction electrons in Au as compared to Co. The magnetic characterization measured with the in-plane magnetic field to the sensor surface for both the as-deposited and annealed multilayers showed isotropic easy axis magnetization parallel to the multilayer interface at a saturating magnetic field of <100 Oersted (Oe). The sensor showed a maximum sensitivity of 5.5×10^4%/RIU (refractive index unit) for water–ethanol media and the highest detection level of 2.5×10^{-6} for water-pentanol media as the protective layer is increased from 0 to 15 nm.

Keywords: Ti/Au/Co/Au; X-ray diffraction; SPR; MOSPR; sensitivity; polycarbonate plastics; protective layer

1. Introduction

Artificially-tailored magneto-optic (MO) Ti/Au/Co/Au structures are interesting materials for investigating magnetic (magnetization, magnetic anisotropy, etc.), microstructure (crystal structure, multilayer interface, surface roughness, etc.), surface plasmon resonance (SPR), and magneto-optics SPR effects arising from the interaction of magnetic field with surface plasmon polariton and correspondingly induced MO properties, and these have huge potential for various applications, for details, see past papers [1–3]. New functionality can be achieved from the combined roles of generating surface plasmon oscillations in the artificially tailored MO structures when excited by a TM polarized (p-polarized) optical radiation that is further controlled by external magnetic, H fields [4]. The excitation condition strongly depends on the magnetic properties such as magnetic permeability and susceptibility, microstructure properties such as metal/dielectric and metal/metal interface states, and dielectric properties such as permittivity of the layers involved [5].

Ti/Au/Co/Au/P_c is one of the most important artificially-tailored MO nanostructured multilayers that has recently seen huge potential in the field of biosensing and imaging [6–9] (t_{pc} denotes the thickness of protective layer here). The choice of Au in this configuration is due to its excellent plasmonic properties arising from the high electron density of about $5.9 \times 10^{22}/cm^3$ (Au possess an abundance of surface plasmons), its low electrical resistivity, and low chemical

reactivity. All these features are essential in reducing attenuation and enhancing plasmon activity. Likewise, the choice of Co as a MO material is due to its excellent H field-dependent property, as pure Co is ferromagnetic with the magnetic moment, μ_B/atom of 0.7 (saturation magnetization, M_s of 172 emu/gm at room temperature), density of 8.9 gm/cm^3, Curie temperature, T_C of 1115 °C, and complex relative permittivity, ε_r of −16.493 + j23.337 at λ = 785 nm (μ_B is the magnetic unit expressed in Bohr unit). Due to the high magnetic moment, it offers the possibility of having the strong magnetic modulation of permittivity at room temperature when excited by an optical radiation near infra-red. By combining plasmonic Au and ferromagnetic Co into Ti buffer and a protective layer, P_c and by optimizing the multilayer configuration, the influence of surface plasmons and magnetism on sensitivity and device performance can be exploited [9–17].

As reported by us earlier [18], the references cited therein, as well as by many others [7,19], several modulation approaches have been explored to enhance the sensitivity of the SPR-based sensors. Depending on the motivation of measurement, two approaches have been employed to investigate the sensitivity of MOKE-based sensors: One is reflectivity change, ΔRp(n) due to modulating H field, and another is normalized reflectivity, again due to modulating magnetic field expressed as, [RpH(+) − RpH(−)]/[RpH(+) + RpH(−)], where RpH(+) and RpH(−) are reflectivity values in the presence of an applied H field in the positive and negative directions, respectively [9,17]. The positive (+) and negative (−) signs denote the direction of applied H field along the +y and –y directions, respectively. In the present case, the MOSPR sensitivity, S_{MOSPR} is calculated using:

$$S_{MOSPR} = \frac{d\left[\frac{R_p(H+) - R_p(H=0)}{R_p(H=0)}\right]}{\Delta n} \times 100 \ [\%/RIU] \quad (1)$$

where $R_p(H=0)$ and $R_p(H+)$ are the reflectivities at the zero and modulating magnetic fields, respectively. Further details on sensitivity are given in Section 5.

Despite the higher sensitivity and improved performances shown by the MO-based SPR sensors, several technical challenges still prevail such as oxidation of sensor surface leading to degradation of performance, issues with reproducibility of the sensor surface due to the difficulty of removing adsorbed materials, and scratching of sensor surface during cleaning. In addition to the composition and layer thickness, interface roughness between each layer of the sensor configuration also plays critical roles in defining MO effect and sensitivity of the sensor [7].

To better understand the light–matter interaction, and magnetic and microstructure properties, in this paper, I explore magneto-optic (MO) Ti/Au/Co/Au/P_c multilayers using quantum design vibrating sample magnetometer/p-MOKE magnetometer and X-ray diffractometers, respectively. I analyze the MO effect using transfer matrix method similar to what has been described in my prior work [20]. Both variations in optical excitation wavelength and probed medium are also taken into consideration in the analysis. Furthermore, I have studied the effect of the protective layer, t_{Pc} (nanosized polycarbonate plastic of permittivity of 2.51 at λ = 785 nm) on the sensitivity and have proposed and demonstrated the practicability of the approach. Three types of alcohol samples, namely, ethanol, propanol, and pentanol with increasing molecular weight and refractive index are used as probing samples. The study shows that the protective layer does not compromise the MO enhancement and sensitivity. The proposed sensor configuration is an excellent candidate for developing robust practical biosensors.

2. Microstructure Study

High angle X-ray diffraction (XRD) or low angle X-ray reflection (XRR) analyses are widely used to characterize many unknown nanostructured materials in the field of geology, environmental science, material science, engineering, and biology, to name a few [21]. While XRD (Rigaku SmartLab, Tokyo, Japan) is primarily used to determine crystal structure, the lattice mismatch between the substrate and individual layers due to stress or strain, dislocation density, and quality of the nanostructure multilayer

films, XRR (Rigaku SmartLab, Tokyo, Japan) is used to determine the layer or bilayer thickness, surface or interface roughness, and density of the film. These studies help us to understand better light–matter interaction and relationship between the crystallographic plane and magneto-optics properties that are essential for biosensing.

Figure 1 shows the high-angle out-of-plane XRD profiles measured for both the as-deposited (shown by blue curve) and annealed (shown by red curve) dc-sputtered Ti/Au/Co/Au configuration corresponding to the (111) textured growth. The profile shows a peak at an average interplanar distance of Co and Au. The high-intensity diffraction peaks indicate the presence of Au (111), Co (111), Au (222), and Au (220) planes parallel to the multilayer interface. As shown in it, the position of peaks slightly shifted towards higher angles after annealing, similarly to our nanoscale Co/Au multilayer reported earlier [22]. However thicker layers showed the signature of Au (222), Co (111), and Co (002) planes in addition to the Au (111) planes. In all the cases, reflection peaks are characteristically sharp and they can be explained using [21] as:

$$2sin\theta_x = \frac{1}{\hat{d}} + \frac{n}{\Lambda} \quad (2)$$

where n is the order of the satellite peaks around the main Bragg peak, $\hat{d}$ is the average interplanar lattice spacing, Λ is the multilayer periodicity/thickness, and θ_x is Bragg's angle. The sharpness of the peak indicates good interface coherence and highly crystalline morphology along the surface normal to the substrate.

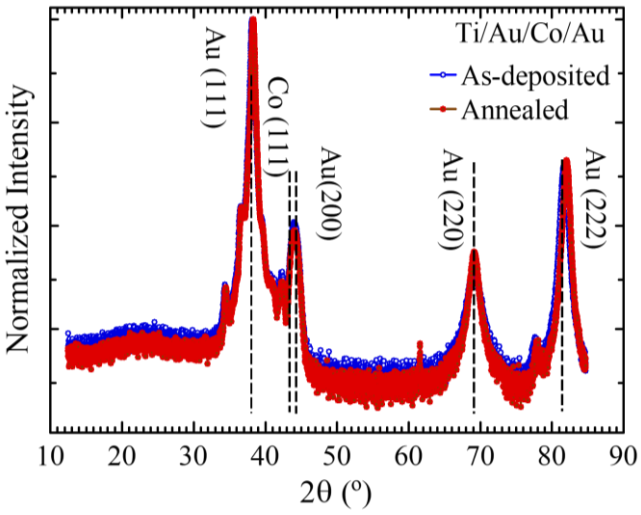

Figure 1. Comparison of high-angle X-ray diffractometer profiles for the as-deposited (denoted by blue) and annealed (denoted by red) Ti/Au/Co/Au multilayers.

Figure 2 shows the results of a low-angle reflectivity (XRR) profiles of Ti/Au/Co/Au structure as analyzed using X-ray diffractometer. The profile shows several peaks at an average interplanar distance of Co and Au and is controlled by the refractive index of Ti, Au, and Co layers. The refractive index is related to the atomic density and scattering power of individual elements, in this case, again, Ti, Au, and Co.

The low angle XRR profiles of the multilayer is dominated by the total thickness since the real parts of the indices of refraction, in this case, are almost equal ($n_{Au} \approx 0.99$, $n_{Co} \approx 0.85$, and $n_{Ti} \approx 0.998 < 1.0$ at the X-ray wavelength, λ of 0.000154 μm [23]). Moreover, the profile is not only depending on the total thickness but also on all four layers and interface states between each of them; this possess problems in separating discrete (ρ_d) from continuous roughness (ρ_c) [24]. Note that the roughness caused by atomic level variation is termed as a continuous roughness and can vary continuously throughout the

multilayer. It can arise from the lattice mismatch at the interface between two layers, dislocation, layer thickness variation, etc. Whereas, discrete roughness is associated with layer thickness consisting of an integer number of atomic layers and it usually results from nonuniform growth modes. The detailed discussion on roughness is beyond the scope of this paper. Interested readers are referred to past papers [24,25]. Overall roughness is given by $\rho = \sqrt{(\rho_c{}^2 + \rho_d{}^2)}$ where, ρ_c and ρ_d are continuous and discrete disorders, respectively. This can also arise from the buffer layer and substrates.

The beating seen in the measured XRR profiles in Figure 2 can arise either from the oxidation of the buffer layer or surface roughness of both buffer layer and substrate. Discrete roughness can also be a cause of the beating. After annealing, the dip in the reflection peaks is further reduced suggesting the improvement of the surface of the buffer layer. For additional information about roughness, I refer interested readers to my prior work [20].

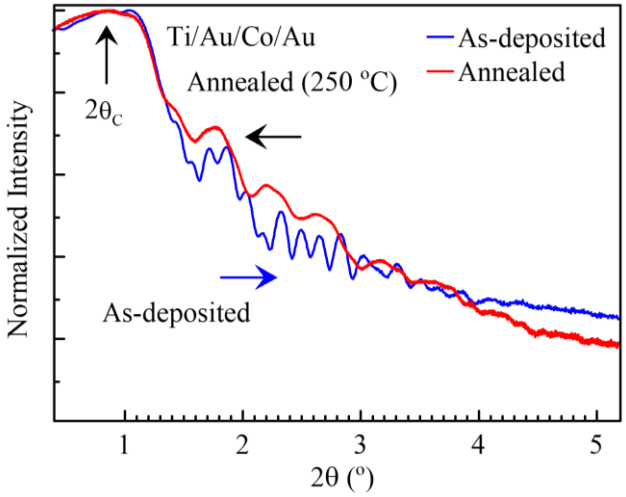

Figure 2. Comparison of X-ray reflection profiles of as-deposited (denoted by blue) and annealed (denoted by red). The blue horizontal arrow shows the direction of increasing roughness. The vertical black arrow shows the position of the critical angle ($2\theta_c$)—the angle above which total internal reflection takes place.

3. Magnetic Characterization

The effect of the interaction of the magnetic field, H with optical radiation for paramagnetic or diamagnetic matter is very small at normal intensities and can be neglected. However, in the present work, in ferromagnetic multilayers consisting of Co, the interaction of light with the magnetic moment of Co has two effects depending on whether the incident optical radiation is TE-polarized (s-polarized) or TM-polarized (p-polarized) with respect to the orientation of magnetic moment. TE-polarized light cannot excite any SPR in the metal/dielectric interface. For the TM-polarized light, a direct relationship exists between the interaction of optical radiation and magnetism (M_s—saturation magnetization) and correspondingly induced dielectric tensor of Co, known as magneto-optic (MO) coefficient. The MO effect is directly related to the orientation of magnetic moment or the direction of the applied field in the sensor configuration and therefore, magnetic measurement is important to understand the physics of light–matter interaction in a multilayer configuration.

If a TM-polarized (p-polarized) light is perpendicularly incident on the sensor surface, the light is purely reflected (this is further discussed in Section 5) meaning that the orientation of magnetic moment in Co has a strong effect on whether the light gets reflected or rotated. Figure 3 shows the normalized M-H curves of the as-deposited and annealed samples, measured with the in-plane magnetic field, H swept between ±10 kOe. The inset in the right shows an enlarged view of the M-H curves, with a coercive force, H_c of 40 Oe. Both the in-plane and perpendicular-to-plane of the tri-layer surface (only in-plane measured M-H curves are shown here) for both the as-deposited and annealed

samples showed isotropic in-plane easy axis magnetization along the multilayer interface. The M_s for the as-deposited structure is found to be 1407 emu/cm^3 and it is decreased to 1233 emu/cm^3 after annealing at 250 °C for 30 min. Unlike our nanoscale Co (1 nm) /Au (2 nm) multilayers reported earlier [21], the M_s in multilayer with 8 nm thick Co layer slightly decreases after annealing. It seems that the interface states between the Au and Co are primarily responsible for this decrease. This information will be very useful in developing a practical biosensor.

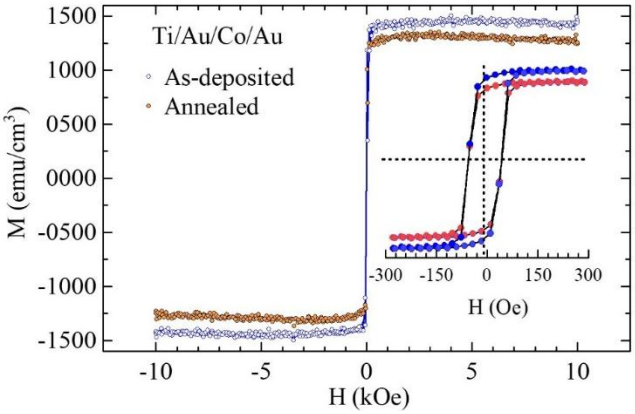

Figure 3. Magnetization (M-H) characteristics of the as-deposited (denoted by blue circles) and annealed (denoted by red circles) samples plotted against the magnetic, H field. The inset shows the enlarged view of the M-H curves measured at H ±300 Oe.

As shown by the M-H curves, the multilayer configuration shows an easy axis along the multilayer surface. That is, the orientation of magnetic moments in the 8 nm thick Co layer are parallel to the interface between Co and Au layers, this configuration is further discussed in Section 5. The magnitude of coercive force (<50 Oe) suggests that only a small amount of H field is needed to saturate the film or to rotate the magnetic spin along the transverse direction, i.e., parallel to the tri-layer interface.

4. MO-SPR Sensitivity and Protective Layer

Figure 4 shows normalized MOSPR sensitivity curves plotted against incident angles with increasing protective layer thickness, t_{Pc} = 0 to 15 nm, calculated in a water-medium in response to three different probing biosamples, namely, ethanol, propanol, and pentanol in an increasing refractive index. The protective layer is an inert and transparent plastic (polycarbonate, in this case) with a permittivity of 2.51 at λ = 785 nm.

Figure 4a shows the normalized MOSPR sensitivity of the sensor without a protective layer i.e., t_{Pc} = 0 nm. The maximum sensitivity occurs at the excitation angle, θ of 41.51° for water–ethanol media. The peak shifts slightly towards higher angle for water–propanol and water–pentanol media, with increasing refractive index change, Δn.

Figure 4b–d show normalized sensitivity as the t_{pc} is increased from 5 to 15 nm (in the increment of 5 nm). The incident angle at which the maximum sensitivity occurs shifts towards higher angles (42.15° → 42.75° → 43.48°) with both increasing t_{pc} (5 → 10 → 15 nm) and Δn (0.0218 → 0.0492 → 0.0732). In this scheme, the magnitude of this sensitivity is strongly dependent on Δn whereas the shift of maximal peak position is dependent on t_{pc}. More importantly, the t_{pc} did not have any adverse effect on the magnitude of sensitivity. In all cases, the MOSPR peaks are sharper and show higher gradients compared to the conventional SPR sensors, meaning increased signal-to-noise ratio when operated either at angular and/or intensity interrogation modes [14].

All the calculated parameters obtained from Figure 4 are listed in Table 1. As shown in it, the maximum MOSPR sensitivity in a water medium is found to be about 5.5 × 10^4%/RIU (refractive index unit) and the highest is for water–ethanol media (i.e., for smaller Δn). This value is almost one

order larger compared to the sensitivity of the SPR-based sensor ($\approx 10^3$%/RIU). SPR sensitivity is not shown here for simplicity. The detection level for the MOSPR sensors increased with increasing Δn of the tested samples and the highest is for water–pentanol media (2.5×10^{-6} RIU). For information on the effect of Co and Au layer thicknesses on the MOSPR sensitivity, I refer interested readers to my prior work [18].

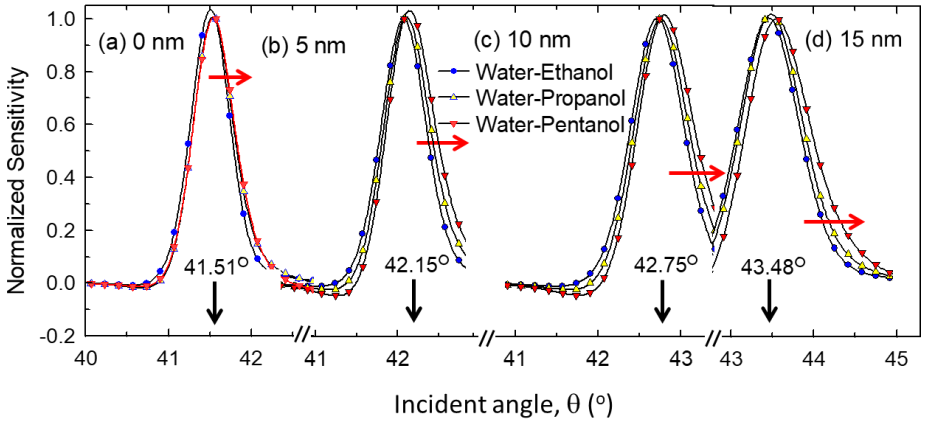

Figure 4. The plot of normalized sensitivity recorded for three different alcohol samples with an increasing refractive index with respect to the water medium. (**a**) Sensor without a protective layer and (**b**–**d**) sensor with a protective layer, increased from 5 to 15 nm. The vertical black arrows indicate the position of reflectivity minima observed for a pure water medium. The red horizontal arrows indicate the direction of peak shift with refractive index change.

Table 1. Optical parameters for water-based media. In column 2, the quantity inside the bracket denotes the thickness of the protective layer, t_{Pc}. In column 3, only the actual sensitivity values calculated for Ti (2 nm)/Au (35 nm)/Co (8 nm)/Au (10 nm)/P_c (t_{pc} = 0 nm) multilayer are shown for three different probing samples. The detection noise, $\sigma = 5.0 \times 10^{-4}$ was obtained from the literature [26], and S_{MOSPR} and D denote sensitivity and detection level, respectively.

Probing Media (Δn at λ = 785 nm)	Incident Angle, θ° and the Numbers within the Bracket Indicate the Thickness of the Protective Layer (t_{pc}), in nm.				Sensitivity, S_{MOSPR} [%/RIU]	Detection Level, $D = \sigma/S_{MOSPR}$ (RIU)
water–ethanol (0.0281)	41.51° (0)	42.15° (5)	42.75° (10)	43.48° (15)	5.5×10^4	0.90×10^{-6}
water–propanol (0.0492)	41.60° (0)	42.20° (5)	42.85° (10)	43.60° (15)	3.2×10^4	1.56×10^{-6}
water–pentanol (0.0732)	41.70° (0)	42.30° (5)	42.95° (10)	43.72° (15)	2.0×10^4	2.50×10^{-6}

5. Materials and Methods

A typical proposed MOSPR sensor configuration is shown in Figure 5. It consists of Au(t_{Au})/Co(t_{Co})/Au(t_{Au}) multilayers including a Ti buffer layer and glass substrate. The samples were prepared by depositing the Ti buffer layer first on a glass substrate and then depositing Au and Co layers using dc-sputtering (AJA International, 809 Country Way, Scituate, MA, USA) at a vacuum pressure of 10^{-6} Torr, and at room temperature, where t_{Ti}, t_{Co}, and t_{Au} denote the thicknesses of Ti, Co, and Au layers, respectively.

The deposition method is as follows. First, a thin buffer layer of 2 nm of Ti (0.03 nm/s) was deposited on to the glass substrate surface; the buffer layer was not annealed. As the next step, a 35 nm of Au layer (0.07 nm/s) was deposited on the Ti buffer layer. After that, an 8 nm of Co (0.03 nm/s) was deposited on top of the Au layer. Finally, a 10 nm of Au layer was deposited on top of the Co layer. For further details on the fabrication method, interested readers are referred to my recent paper [20]. Various geometrical and optical parameters are given in Table 2.

The M-H curves were measured using a Quantum Design vibrating sample magnetometer and a p-MOKE magneto-meter (VersaLab Quantum Design, San Diego, CA, USA) with H swept at ±10 kOe for both the as-deposited and annealed samples. The microstructure was investigated using X-ray diffractometer at both low and high angles. Theoretical fittings of the experimental data using *GenX* [27] was also performed but these are not shown here for simplicity. For further details on data fitting on similar structures, I refer interested readers again, to my prior work [21].

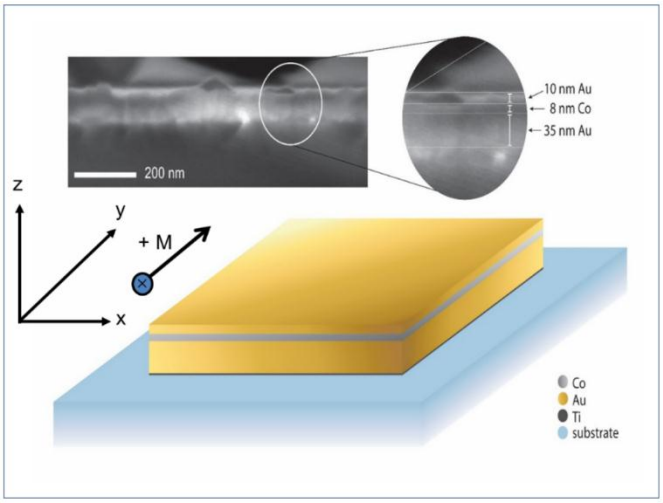

Figure 5. Schematic of a fabricated sensor configuration (bottom). Shown on the top left is the side view of the fabricated sensor studied using SEM (FEI Apreo SEM, ThermoFisher Scientific, Hillsboro, OR, USA). Enlarged view is shown on the top right. The orientation of magnetic spin is shown by a large thick arrow that is parallel to the Co/Au interface. A positive direction of applied H field is assumed to be along the direction shown by the long thick arrow (i.e., +y-axis).

Table 2. Optical parameters at λ = 785 nm used for modeling. ε_{moCo} is the complex magneto-optic constant of Co, also known as off-diagonal tensor component ($\varepsilon_{moCo} = -0.85 + j0.0006$ at λ = 785 nm), obtained from a past paper [5].

Materials	Symbol	Refractive Index, n	Extinction Coeff., k	Real Part, ε_1	Imaginary Part, ε_2	Literature Source
Optical Glass	BK-7	1.5111	9.22×10^{-9}	2.30	2.95×10^{-9}	[28]
Titanium	Ti	3.0937	4.01	−6.51	24.811	[29]
Gold	Au	0.14891	4.78	−22.86	1.4245	[29]
Cobalt	Co	2.4580	4.75	−16.49	23.337	[29]
Air	Air	1.000275	-	1.0055	-	[30]
Water	H_2O	1.3296	1.39×10^{-7}	1.7678	3.69×10^{-9}	[31]
Ethanol	C_2H_5OH	1.3577	-	1.8433	-	[32]
Propanol	C_3H_7OH	1.3788	-	1.9011	-	[33]
Pentanol	$C_5H_{11}OH$	1.4028	-	1.9678	-	[33]
Polycarbonate	$(C_{16}H_{14}O_3)_n$	1.5713	-	2.51	-	[34]

For the MO characterizations, the multilayer structure shown in Figure 5 was optically interfaced to a prism in Kretschmann configuration using an index matching fluid (i.e., matching liquid) between the glass substrate and prism surface, similarly to the configuration shown previously [20]. The surface plasmon was excited using TM-polarized (p-polarized) optical radiation at an λ of 785 nm. In this work, the optical constants were obtained from the literature (see, column 7 in Table 2). The MO coefficient (ε_{moCo}) for Co was obtained from the literature [5]. The ε_{moCo} was set to zero and the literature value under zero and saturating H fields, respectively. The various dimensional and optical parameters used in the calculations and correspondingly cited references are listed in Table 2.

For the sensitivity calculation, the change in reflectivity due to the modulating H field was normalized as $\left[\frac{R_p(H+) - R_p(H=0)}{R_p(H=0)}\right]$ for the water medium and the same was done for ethanol, propanol, and pentanol media. The MOSPR sensitivity for water–ethanol media was calculated using

$$\frac{\left[\frac{R_p(H+) - R_p(H=0)}{R_p(H=0)}\right]_{\text{Ethanol}} - \left[\frac{R_p(H+) - R_p(H=0)}{R_p(H=0)}\right]_{\text{Water}}}{\Delta n} \times 100\ [\%/\text{RIU}] \quad (3)$$

where Δn is the change in refractive index between ethanol (probing sample) and reference sample (water, in this case). The same calculation was repeated for water–propanol and water–pentanol media for all protective layer thicknesses (t_{pc} = 0, 5, 10, and 15 nm). The positive (+) sign denotes the direction of an applied H field (+y axis). This is indicated by a long dark arrow in Figure 5.

6. Conclusions

I experimentally investigated the microstructural and magnetic properties of magneto-optical (MO) Ti/Au/Co/Au/P_c biosensor. Microstructure studies showed strong fcc-Au <111> phase for all the fabricated samples. Magnetic studies suggested isotropic behavior with an easy axis parallel to the Co/Au interface. The MO configuration showed a maximum sensitivity of 5.5×10^4%/RIU (water–ethanol media). The protective layer does not compromise the sensitivity of the sensor. The highest detection level is found to be 2.5×10^{-6} RIU (water–pentanol media), which is comparable to or larger than the sensitivity of the recently reported SPR sensors for liquid media [18]. This work opens the possibility of developing a robust and practical biosensor with increased lifetime, and improved detection level and sensor performance.

Funding: This work was supported in part by the Centre for Memory and Recording Research at UC San Diego, CA, USA, in part by the Natural Sciences and Engineering Research Council, and in part by MITACS Inc., of Canada.

Acknowledgments: The author thanks James Wingert (member of the Shpyrko Group, Department of Physics, University of California, San Diego, CA, USA) for X-ray characterization, Mathew Rozin (member of the Tao Group, Department of Nanoengineering, University of California, San Diego, CA, USA) for SEM imaging, and Frederick E. Spada (Associate Research Scientist, Center for Memory and Recording Research (CMRR), University of California, San Diego, CA, USA) for granting an access to the polar-MOKE device for magnetic characterization. The author acknowledges the financial support received from NSERC and MITACS Inc. (Vancouver, BC, Canada) and CMRR (UC San Diego, CA, USA) for this work.

Conflicts of Interest: The author declares no conflict of interest.

References

1. Rizal, C.; Niraula, B.; Lee, H.H.W. Bio-magnetoplasmonics, emerging biomedical technologies and beyond. *J. Nanomed. Res.* **2016**, *3*, 00059–00065. [CrossRef]
2. Rizal, C.; Moa, B.; Niraula, B.B. Ferromagnetic multilayers: Magnetoresistance, magnetic anisotropy, and beyond. *Magnetochemistry* **2016**, *2*, 22. [CrossRef]
3. Kushwaha, M.S.; Halevi, P. Magnetoplasmons in thin films in the Voigt configuration. *Phys. Rev. B* **1987**, *36*, 5960–5967. [CrossRef]
4. Diaz-Valencia, B.; Mejía-Salazar, J.; de Oliveira, O.N., Jr.; Porras-Montenegro, N.; Albella, P. Enhanced transverse magneto-optical Kerr effect in magnetoplasmonic crystals for the design of highly sensitive plasmonic (bio) sensing platforms. *ACS Omega* **2017**, *2*, 7682–7685. [CrossRef] [PubMed]
5. González-Díaz, J.; Sepúlveda, B.; García-Martín, A.; Armelles, G. Cobalt dependence of the magneto-optical response in magnetoplasmonic nanodisks. *Appl. Phys. Lett.* **2010**, *97*, 043114. [CrossRef]
6. Armelles, G.; Cebollada, A.; Garcia-Martan, A.; González, M.U. Magnetoplasmonics: Combining magnetic and plasmonic functionalities. *Adv. Opt. Mater.* **2013**, *1*, 2–21. [CrossRef]
7. Manera, M.G.; Ferreiro-Vila, E.; Garcia-Martin, J.M.; Garcia-Martin, A.; Rella, R. Enhanced antibody recognition with a magneto-optic surface plasmon resonance (MO-SPR) sensor. *Biosens. Bioelectron.* **2014**, *58*, 114–120. [CrossRef] [PubMed]

8. Papaioannou, E.T.; Karoutsos, V.; Angelakeris, M.; Valassiades, O.; Fumagalli, P.; Flevaris, N.K.; Poulopoulos, P. Magnetic, magneto-optic and magnetotransport properties of nanocrystalline Co/Au multilayers with ultrathin Au interlayers. *J. Nanosci. Nanotechnol.* **2008**, *8*, 4323–4327. [CrossRef] [PubMed]
9. Regatos, D.; Sepúlveda, B.; Fariña, D.; Carrascosa, L.G.; Lechuga, L.M. Suitable combination of noble/ferromagnetic metal multilayers for enhanced magneto-plasmonic biosensing. *Opt. Express* **2011**, *19*, 8336–8346. [CrossRef] [PubMed]
10. Herreño-Fierro, C.A.; Patino, E.J.; Armelles, G.; Cebollada, A. Surface sensitivity of optical and magneto-optical and ellipsometric properties in magnetoplasmonic nanodisks. *Appl. Phys. Lett.* **2016**, *108*, 021109. [CrossRef]
11. Špringer, T.; Ermini, M.L.; Špačková, B.; Jabloňkůa, J.; Homola, J. Enhancing sensitivity of surface plasmon resonance biosensors by functionalized gold nanoparticles: Size matters. *Anal. Chem.* **2014**, *86*, 10350–10356. [CrossRef] [PubMed]
12. Wang, T.-J.; Lee, K.-H.; Chen, T.-T. Sensitivity enhancement of magneto-optic surface plasmon resonance sensors with noble/ferromagnetic metal heterostructure. *Laser Phys.* **2014**, *24*, 036001. [CrossRef]
13. Pellegrini, G.; Mattei, G. High-performance magneto-optic surface plasmon resonance sensor design: An optimization approach. *Plasmonics* **2014**, *9*, 1457–1462. [CrossRef]
14. Piliarik, M.; Homola, J. Surface plasmon resonance (SPR) sensors: Approaching their limits? *Opt. Express* **2009**, *17*, 16505–16517. [CrossRef] [PubMed]
15. Slavík, R.; Homola, J. Ultrahigh resolution long range surface plasmon-based sensor. *Sens. Actuators B* **2007**, *123*, 10–12. [CrossRef]
16. Sepúlveda, B.; Calle, A.; Lechuga, L.M.; Armelles, G. Highly sensitive detection of biomolecules with the magneto-optic surface-plasmon-resonance sensor. *Opt. Lett.* **2006**, *31*, 1085–1087. [CrossRef] [PubMed]
17. D'Amico, A.; Di Natale, C. A contribution on some basic definitions of sensors properties. *IEEE Sens. J.* **2001**, *1*, 183–190. [CrossRef]
18. Rizal, C.; Pisana, S.; Hrvoic, I. Improved magneto-optic surface plasmon resonance biosensors. *Photonics* **2018**, *5*, 15. [CrossRef]
19. Konopsky, V.N.; Basmanov, D.V.; Alieva, E.V.; Dolgy, D.I.; Olshansky, E.D.; Sekatskii, S.K.; Dietler, G. Registration of long-range surface plasmon resonance by angle-scanning feedback and its implementation for optical hydrogen sensing. *New J. Phys.* **2009**, *11*, 063049. [CrossRef]
20. Rizal, C.; Pisana, S.; Hrvoic, I.; Fullerton, E. Microstructure and magneto-optical surface plasmon resonance of Co/Au multilayers. *J. Phys. Commun.* **2018**, *2*, 055010. [CrossRef]
21. Rizal, C.; Fullerton, E. Perpendicular magnetic anisotropy and microstructure properties of nanoscale Co/Au multilayers. *J. Phys. D Appl. Phys.* **2017**, *50*, 355002. [CrossRef]
22. Rizal, C.; Moa, B.; Wingert, J.; Shpyrko, O.G. Magnetic anisotropy and magnetoresistance properties of Co/Au multilayers. *IEEE Trans. Magn.* **2015**, *51*, 1–6. [CrossRef]
23. RefractiveIndex.INFO—Refractive Index Database. Available online: https://refractiveindex.Info/ (accessed on 8 June 2018).
24. Fullerton, E.E.; Schuller, I.K.; Vanderstraeten, H.; Bruynseraede, Y. Structural refinement of superlattices from x-ray diffraction. *Phys. Rev. B* **1992**, *45*, 9292. [CrossRef]
25. Heinrich, B.; Bland, J.A.C. *Ultrathin Magnetic Structures II: Measurement Techniques and Novel Magnetic Properties*; Springer Science & Business Media: Berlin, Germany, 2006.
26. Ignatyeva, D.O.; Knyazev, G.A.; Kapralov, P.O.; Dietler, G.; Sekatskii, S.K.; Belotelov, V.I. Magneto-optical plasmonic heterostructure with ultranarrow resonance for sensing applications. *Sci. Rep.* **2016**, *6*, 28077. [CrossRef] [PubMed]
27. Björck, M.; Andersson, G. Genx: An extensible x-ray reflectivity refinement program utilizing differential evolution. *J. Appl. Crystallogr.* **2007**, *40*, 1174–1178. [CrossRef]
28. SCHOTT Advanced Optics. Available online: https://www.schott.com/advanced_optics/english/download/ (accessed on 2 June 2018).
29. Johnson, P.; Christy, R. Optical constants of transition metals: Ti, V, Cr, Mn, Fe, Co, Ni, and Pd. *Phys. Rev. B Condens. Matter* **1974**, *9*, 5056. [CrossRef]
30. Ciddor, P.E. Refractive index of air: New equations for the visible and near infrared. *Appl. Opt.* **1996**, *35*, 1566–1573. [CrossRef] [PubMed]

31. Hale, G.M.; Querry, M.R. Optical constants of water in the 200-nm to 200-µm wavelength region. *Appl. Opt.* **1973**, *12*, 555–563. [CrossRef] [PubMed]
32. Rheims, J.; Köser, J.; Wriedt, T. Refractive-index measurements in the near-IR using an abbe refractometer. *Meas. Sci. Technol.* **1997**, *8*, 601. [CrossRef]
33. Moutzouris, K.; Papamichael, M.; Betsis, S.C.; Stavrakas, I.; Hloupis, G.; Triantis, D. Refractive, dispersive and thermo-optic properties of twelve organic solvents in the visible and near-infrared. *Appl. Phys. B* **2014**, *116*, 617–622. [CrossRef]
34. Sultanova, N.; Kasarova, S.; Nikolov, I. Dispersion properties of optical polymers. *Acta Phys. Pol. A* **2009**, *116*, 585. [CrossRef]